Atmos. Chem. Phys. Discuss., 9, 22883–22927, 2009
www.atmos-chem-phys-discuss.net/9/22883/2009/

Atmospheric Chemistry and Physics Discussions

This discussion paper is/has been under review for the journal *Atmospheric Chemistry and Physics (ACP)*. Please refer to the corresponding final paper in *ACP* if available.

Volume nucleation rates for homogeneous freezing in supercooled water microdroplets: results from a combined experimental and modelling approach

M. E. Earle[1,*], T. Kuhn[1,], A. F. Khalizov[1,***], and J. J. Sloan[1]**

[1]Department of Earth and Environmental Sciences, University of Waterloo, Waterloo, ON, Canada
[*]now at: Cloud Physics and Severe Weather Research Section, Environment Canada, Toronto, ON, Canada
[**]now at: Department of Space Science, Lulea Technical University, Kiruna, Sweden

[***]now at: Department of Atmospheric Sciences, Texas A&M University, College Station, TX, USA

Received: 28 August 2009 – Accepted: 13 October 2009 – Published: 28 October 2009

Correspondence to: J. J. Sloan (sloanj@uwaterloo.ca)

Published by Copernicus Publications on behalf of the European Geosciences Union.

Abstract

Temperature-dependent volume nucleation rate coefficients for supercooled water droplets, $J_V(T)$, are derived from infrared extinction measurements in a cryogenic laminar aerosol flow tube using a microphysical model. The model inverts water and ice aerosol size distributions retrieved from experimental extinction spectra by considering the evolution of a measured initial droplet distribution via homogeneous nucleation and the exchange of vapour-phase water along a well-defined temperature profile. Experiment and model results are reported for supercooled water droplets with mode radii of 1.0, 1.7, and 2.9 μm. Values of mass accommodation coefficients for evaporation of water droplets and vapour deposition on ice particles are also determined from the model simulations. The coefficient for ice deposition was found to be approximately 0.031, while that for water evaporation was 0.054. Results are considered in terms of the applicability of classical nucleation theory to the freezing of micrometre-sized droplets in cirrus clouds, with implications for the parameterization of homogeneous ice nucleation in numerical models.

1 Introduction

Cirrus clouds play a significant role in Earth's radiative balance due to their interactions with incident solar and surface-emitted thermal radiation (Liou, 1986). The radiative influence of cirrus clouds is predicated on the concentrations, sizes, and shapes of the constituent ice particles (Lawson et al., 2006). Microphysical schemes in numerical models used to quantify and predict this influence require detailed parameterizations of the processes involved in ice initiation. Primary ice formation by homogeneous and/or heterogeneous nucleation provides an important starting point for describing the evolution of cloud properties due to mass-transfer evaporation/growth (the Bergeron-Findeisen process) and agglomeration/riming. Thus, ice nucleation processes in cirrus clouds continue to be an active area of atmospheric research.

At temperatures below about 235 to 237 K, cirrus ice is formed primarily by homogeneous nucleation of aqueous droplets (Heymsfield et al., 2005). In the classical approach, homogeneous nucleation is considered to occur within the bulk volume of an aqueous droplet (Turnbull and Fisher, 1949), with a temperature-dependent rate coefficient, $J_V(T)$, having units of $\mathrm{cm}^{-3}\,\mathrm{s}^{-1}$. Numerous laboratory studies have been conducted to determine atmospherically-relevant values of the nucleation rate coefficient. The bulk of this experimental work has focussed on the freezing of pure water droplets as a model system for ice formation in cirrus clouds and as a fundamental testing ground for the predictions of classical nucleation theory. Using water droplets suspended in air (Demott and Rogers, 1990; Duft and Leisner, 2004; Krämer et al., 1999; Stöckel et al., 2005) and various oils (Butorin and Skripov, 1972; Taborek, 1985), values of $J_V(T)$ were determined from experimental measurements employing a range of droplet sizes and freezing detection methods.

The experimentally-determined rate coefficients from the pure water studies are in general agreement with classical nucleation theory (Pruppacher, 1995). In some instances, however, there are large discrepancies among the results obtained from different studies; for example, there is a spread of over five orders of magnitude in values obtained at 240 K (Tabazadeh et al., 2002b). For some time, it has been unclear whether these large discrepancies were due solely to systematic differences in the experimental techniques and/or errors, or to some deficiency in the classical, volume-based approach for deriving nucleation rate coefficients from freezing data. The latter notion has been discussed recently, following the proposal that in some cases, crystal nucleation at the droplet surface is thermodynamically favoured over nucleation within the bulk volume (Djikaev et al., 2002; Tabazadeh et al., 2002a, b). The thermodynamic basis for surface nucleation is the potential decrease in surface energy when at least one of the crystal faces is in contact with the surrounding medium (air or oil in the relevant experimental studies), rather than the bulk liquid. The corresponding dependence on droplet surface area necessitates the introduction of a second, surface-specific rate coefficient, $J_S(T)$, with units of $\mathrm{cm}^{-2}\,\mathrm{s}^{-1}$.

The total nucleation rate, J_t, has units of s^{-1} and is the sum of contributions from volume- and surface-based processes:

$$J_t = J_V V + J_S S \quad (1)$$

where V and S are the volume and surface area of the droplets, respectively. The relative contributions of each nucleation process depend on the nature of the interface with the droplet (air or oil) and droplet size (Tabazadeh et al., 2002b). The contribution of surface nucleation is expected to increase with decreasing particle size, because of the increasing surface-to-volume ratio. Duft and Leisner (2004) determined J_V values for 19 and 49 μm (radius) droplets levitated (in air) in an electrodynamic balance, and suggested that surface nucleation will only be important for particles with radii less than about 4 μm.

To assess further whether the classical, volume-based theory for homogeneous nucleation can be extended to micrometre-sized droplets suspended in air, additional laboratory studies are required. The evaporation of droplets in electrodynamic balances is prohibitive to the determination of $J_V(T)$ values for small droplets. Aerosol flow tubes (AFTs) and cloud chambers provide avenues for laboratory studies of micrometre-sized droplets; however, the determination of nucleation rate coefficients is complicated by the evaporation of liquid droplets and subsequent deposition on ice particles. This water vapour mass transfer growth of ice particles leads to increases in the (volume) ice fraction which are not directly related to the nucleation process. Previous studies of homogeneous ice nucleation in aerosol flow tubes have shown that at temperatures near the nucleation point, only a small fraction of the aerosols freeze (1 in 10^4 to 10^6), followed by significant vapour-phase exchange from the remaining liquid droplets to the nascent ice particles (Chelf and Martin, 2001).

To separate the contributions from homogenous nucleation and water vapour mass transfer in experimental measurements of aerosols in laminar flow tubes, microphysical models have been employed. Hung and Martin (2001) developed an inversion model in which the volume-based nucleation rate was treated as an adjustable parameter,

and homogeneous nucleation and mass transfer were considered as sequential processes. The nucleation rate, $J_V(T)$, was varied iteratively to produce the best agreement between the volume fraction of ice calculated by the model, and that determined by Fourier-transform infrared (FTIR) observation, for a given freezing temperature.

The objective of this study is to combine experimental measurements from an aerosol flow tube with a microphysical model to determine $J_V(T)$ for micrometre-sized water droplets. The AFT apparatus has been characterized extensively using computational fluid dynamic (CFD) calculations (Khalizov et al., 2006b). Laminar flow conditions were demonstrated by quantifying thermal transfer in the flowing gas, thereby providing a time scale for kinetic measurements. The experimental conditions were designed to be appropriate for the application of the results to cirrus cloud formation. The microphysical model used in this study treats nucleation and mass transfer as simultaneous processes, thereby differing from the sequential approach used in previous models. This paper details the experimental setup and approach, as well as the design and implementation of the model. Values of $J_V(T)$ are reported from model simulations for pure water droplets with mode radii (maxima in the volume size distributions) of 1.0, 1.7, and 2.9 μm. The results are considered with respect to the applicability of classical, volume-based, nucleation theory to the freezing of small droplets in cirrus clouds. The implications for bulk parameterizations of homogeneous nucleation in numerical models are also discussed.

2 Experimental

2.1 Freezing experiments

Freezing experiments were performed in a vertical aerosol flow tube (AFT), the details of which have been reported elsewhere (Khalizov et al., 2006a). The tube is equipped with copper cooling coils capable of operation down to 150 K, and was designed to maintain laminar conditions with no temperature gradient-driven recirculation

under very low flow velocities. It comprises four independently temperature-controlled copper sections, each 37.5 cm long, with an inner diameter (i.d.) of 8.9 cm. Adjacent sections are joined by thin-walled stainless steel bellows, which minimize heat flow and allow individual sections to be maintained at different temperatures. The inner assembly (copper sections and bellows) is enclosed within an evacuated stainless steel jacket that provides thermal isolation from the laboratory environment. Chilled nitrogen coolant (mixture of liquid and gas) flows through coils affixed to the outer wall of each section. The wall temperature of each section is regulated using a LabVIEW® interface and feedback loop that controls a heater in the coolant gas flow. This system can maintain the average temperature of a section within ±0.1 K of the set point value, with axial temperature deviations along the length of each section wall typically maintained within ±0.5 K. A set of cross-shaped copper fins is placed inside each section to transfer heat across the flow tube more efficiently, improving the cooling efficiency and minimizing radial temperature gradients in the gas flow.

A liquid water aerosol was generated by atomization or ultrasonic nebulization of Millipore®-filtered water, or by the heterogeneous condensation of humidified carrier gas on ∼20 nm dry sodium chloride (NaCl) particles. In the latter case, the condensation nuclei were produced by atomizing a dilute, 10^{-4} mol L^{-1} (M) solution of reagent-grade NaCl (Sigma-Aldrich Co.) in Millipore®-filtered water, and passing the aqueous particles through a 60 cm long Nafion® diffusion dryer. The dry salt aerosol was premixed with humidified nitrogen and introduced to the flow tube, where the salt particles deliquesced and continued to grow by water vapour uptake. The low NaCl concentration in the resulting droplets affected neither optical properties (Demott and Rogers, 1990) nor freezing temperatures. We confirmed this in separate freezing experiments with NaCl solutions of several increasing concentrations. Changes in the optical and freezing properties became noticeable only for NaCl concentrations three orders of magnitude higher than those used here.

The experimental configuration is shown in Fig. 1. For each generation method, the droplets or nuclei were entrained in a dry nitrogen gas flow of 3 SLPM (3 L min^{-1} at standard conditions of 294 K and 1013 hPa). These externally-generated particles were introduced at the top of the cryogenic AFT via a central inlet (heated to prevent ice deposition), where they were then combined with a pre-cooled flow of nitrogen carrier gas at 7 SLPM. When employing nebulization or atomization, dry nitrogen carrier gas was used. A mixture of dry (4 SLPM) and humidified (3 SLPM) nitrogen was used for the carrier flow when generating aerosol particles by heterogeneous condensation. The total flow rate was 10 SLPM in all cases.

The aerosol samples were exposed to well-defined temperature profiles as they flowed through the four tube sections, which will be designated A through D (top to bottom) in the following. Sections A and B were maintained at 240 K in all experiments to condition the aerosol. At the end of section B, the samples were composed solely of supercooled droplets. Tube sections C and D were then cooled to candidate freezing temperatures between 230 and 240 K. At a total flow rate of 10 SLPM, the residence time of aerosol particles, from the point at which they are cooled following conditioning to the observation point (see Sect. 2.2), is about 35 s.

2.2 Infrared spectra and retrieval

Infrared (IR) extinction spectra of the flowing aerosol were recorded in the lower half of section D. A collimated IR beam, modulated at 40 kHz metrology frequency by a Michelson interferometer (Bruker Tensor 37), was passed through optical ports (capped with KRS-5 windows) on opposite sides of the flow tube, intersecting the aerosol. The transmitted IR beam was focussed by an off-axis parabolic mirror onto a mercury cadmium telluride (MCT) detector (FTIR-22-1.0, Infrared Associates). For each measurement, 80 scans were averaged over the frequency range from 450 cm^{-1} to 6000 cm^{-1}, at 2 cm^{-1} resolution. Water vapour spectra recorded at 243 K were routinely subtracted from the measured extinction spectra to remove water vapour interference.

A remote sensing retrieval procedure developed in our laboratory was used to determine the phase composition and corresponding size distribution(s) of the supercooled water and/or ice particles from their IR spectra (Zasetsky et al., 2004a, 2007). The retrieval procedure is based on a minimization of the variance between the measured spectrum and a calculated spectrum that is the linear combination of a set of monodisperse reference spectra. This basis set of reference spectra is calculated for 96 radii that are equally spaced on a logarithmic size scale in the range between 0.05 and 11.8 μm. Spectral basis sets for both supercooled water and ice are calculated using Mie scattering code (Bohren and Huffman, 1983), with frequency-dependent complex indices of refraction (Zasetsky et al., 2005). This approach assumes sphericity, which is a reasonable approximation, because the average particle radii are in the 1 μm to 5 μm range and images made with an optical microscope (Zasetsky et al., 2007) mounted temporarily in the aerosol flow (in tube section D) show that under the conditions of these experiments, the particles have near-unity aspect ratios.

The retrieval procedure determines a particle size distribution using a nonlinear least-squares algorithm. The resulting size distribution is the number concentration of particles in each of the 96 size bins (corresponding to the radii in the basis set) which produce the calculated spectrum that best fits the measured spectrum. Ice and/or supercooled water particle distributions are obtained simultaneously in this way. Number size distributions can be converted to volume size distributions by multiplying the number concentration of particles in each bin by $(4/3)\pi r^3$, where r is the bin radius. Volume size distributions are used in all analyses because they are directly related to mass, which is conserved in kinetic processes.

2.3 Initial aerosol size distributions

To estimate the sizes of the conditioned aerosols from each generation method, experiments were conducted with all four flow tube sections held at the conditioning temperature of 240 K. Excess water vapour was removed to the wall and fins by diffusion/condensation upon cooling in the first two sections, and the particles did not

experience appreciable changes in size beyond this point. Analysis of the resulting extinction spectra using the characterization procedure (detailed in Sect. 2.2) produced the volume size distributions of supercooled water droplets for each generation method shown in Fig. 2. The conditioned aerosols produced by heterogeneous condensation have radii between approximately 0.4 and 2 μm, with a maximum in the volume distribution (mode) at about 1 μm. Those produced by the constant output atomizer have radii between 0.6 and 5 μm, with a mode of approximately 1.7 μm. Nebulization produces conditioned aerosols with radii between 1 and 7 μm, with a mode of about 2.9 μm. Based on these sizes, the aerosols produced by condensation, atomization, and nebulization will henceforth be referred to as small, medium, and large droplets, respectively.

2.4 Axial temperature profiles

The axial temperature profile experienced by the aerosol cannot be inferred solely from measurements made at the tube wall and/or at fixed radial positions in the flow (e.g. in the centre), because even at the relatively low linear flow velocities of our experiments (a few cm per second), thermal transfer is not fast enough to equalize the radial temperatures completely. It is necessary to account for these radial temperature gradients (which vary with axial distance along the tube) because the aerosol is spread out over the entire cross-section of the flow. To quantify these gradients, CFD calculations were used to determine the cross-sectional- and mass-averaged temperature profiles in the AFT (Khalizov et al., 2006a). It has been shown that CFD computations accurately represent the conditions to which the aerosol particles are exposed as they travel through the AFT, including not only the temperature distributions, but also important flow characteristics such as gas streamlines and particle tracks. These results show that the particle motion is linear and follows the gas flow, which is laminar under the conditions of our experiments. Laminar flow is necessary both to avoid agglomeration and to ensure that the timescales used in the subsequent kinetic analyses are correct.

CFD profiles were calculated for each candidate freezing temperature. Using the calculated aerosol flow velocities (e.g. $\sim 3\,\mathrm{cm\,s^{-1}}$ for a total flow rate of 10 SLPM), the temperature profiles as a function of the axial coordinate were converted into profiles as a function of aerosol residence time. The latter profiles are required by the kinetic model to interpret the aerosol transformations during freezing. This model is detailed in the following section.

3 Model description

Implemented in Matlab (The Mathworks, Inc.), the model uses volume distributions of supercooled water and ice aerosol particles obtained from freezing experiments to determine temperature-dependent homogeneous nucleation rate coefficients. The distributions measured at different temperatures represent the aerosol particles at the various stages of the freezing event. Before freezing, the initial distribution is that of a pure (supercooled) water aerosol that has been conditioned with all wall temperatures set to 240 K (Fig. 2). The final supercooled water and/or ice distributions are taken from experiments conducted with the bottom two tube sections (C and D) at a given candidate freezing temperature.

The model has two components: a microphysical simulation and a minimization step. The microphysical component consists of a series of rate processes describing homogeneous ice nucleation and (diffusion-limited) exchange between aerosol particles and water vapour. The exchange accounts for mass transfer between the liquid and frozen particles via evaporation, diffusion, and condensation/deposition. All processes use temperature-dependent rate constants and include the influence of the Kelvin effect. Nucleation and vapour-phase exchange processes are considered simultaneously, as opposed to the sequential approach used previously in similar models (Chelf and Martin, 2001; Hung et al., 2002; Hung and Martin, 2001). Beginning with the initial supercooled water aerosol distribution, the microphysical component solves the time-dependent differential equations describing the relevant rate processes, subject to the

axial AFT temperature profile and the nucleation rate function $J_V(T)$. The calculations produce time-dependent volume distributions of supercooled water and/or ice. The normalized sum of squares of differences, χ, between the calculated and measured (in AFT section D) supercooled water and ice distributions is minimized by varying the function $J_V(T)$.

3.1 Details of microphysical component

The volume distributions of supercooled water and ice output by the retrieval procedure (Sect. 2.2) give the volume concentration of particles in each of the 96 size bins corresponding to the radii specified in the spectral basis set. These radii will be referred to as nodes in the following. Particles in the size bins are assumed to reside only at the nodes.

The rate of increase in the number of ice particles in node i, N_i^s, due to homogeneous nucleation is given by the following:

$$dN_i^s/dt = N_i^l J_V(T)\, v_i \tag{2}$$

where N_i^l is the number concentration of liquid droplets in node i, and $v_i = (4/3)\,\pi \left(r_i^l\right)^3$ is the volume of a liquid droplet in node i having radius r_i^l. The decrease in the number of water droplets resulting from homogeneous nucleation is determined from the increase in the number of ice particles:

$$dN_i^s/dt = -dN_i^l/dt \tag{3}$$

Equations (2) and (3) are based on the assumptions that nucleation events in droplets are independent, that ice formation is the result of only one nucleation event per droplet, and that once nucleated, the entire droplet is frozen instantaneously.

The temperature dependence of the nucleation rate is given by classical nucleation theory (Turnbull and Fisher, 1949):

$$J_V(T)=N_V\frac{kT}{h}\exp\left(-\frac{\Delta F_V}{kT}\right) \quad (4)$$

where $N_V=3.35\times10^{22}\,\mathrm{cm}^{-3}$ is the number concentration of water molecules in the droplet volume, k is the Boltzmann constant, and h is the Planck constant. The term ΔF_V represents the sum of the free energy of nucleus formation in the bulk volume and the activation energy for the diffusion of water molecules across the liquid–solid boundary of the nucleus (Pruppacher and Klett, 1998; Turnbull and Fisher, 1949). The temperature dependence of J_V is given by the strong temperature dependence of the exponential factor, as well as that of the pre-factor and ΔF_V. The latter was modelled using the expression $\Delta F_V=A_V-B_VT$. Incorporating the parameters A_V (in units of energy) and B_V (in units of energy divided by temperature) into the formulation of $J_V(T)$ used in the model (Eq. 4) gives:

$$J_V(T)=N_V\frac{kT}{h}\exp\left(-\frac{A_V-B_VT}{kT}\right) \quad (5)$$

The temperature dependence in Eq. (5) governs the number of ice particles formed as the temperature of the supercooled water aerosol changes subject to the temperature profile in the flow tube. Minimization of the function χ by varying the parameters A_V and B_V produces the temperature-dependent nucleation rates $J_V(T)$ that are the desired output.

Diffusion-limited exchange processes result from differences between the saturation vapour pressures above particles and the partial pressure of water vapour in the surrounding gas. These processes include the evaporation and condensation growth of the liquid particles and the deposition growth of the ice particles. The rate of radius change for water droplets and ice particles by the combination of these processes is

determined as follows (Hinds, 1999):

$$\frac{dr_i^l}{dt}=\frac{D_v^*(r_i^l)\,M_\mathrm{w}}{R\,\rho_\mathrm{w}}\frac{1}{r_i^l}\left(\frac{p_\infty}{T_\infty}-\frac{p_i}{T_i^l}\right) \quad (6)$$

$$\frac{dr_i^s}{dt}=\frac{D_v^*(r_i^s)\,M_\mathrm{w}}{R\,\rho_\mathrm{ice}}\frac{1}{r_i^s}\left(\frac{p_\infty}{T_\infty}-\frac{p_\mathrm{ice}}{T_i^s}\right) \quad (7)$$

where r_i^l is the radius of liquid droplets in node i; r_i^s is the radius of ice particles in node i; $D_v^*(r_i^l)$ and $D_v^*(r_i^s)$ are the gas-phase diffusion coefficients for water and ice; M_w is the molar mass of water; R is the ideal gas constant; ρ_w is the density of supercooled water; ρ_ice is the density of ice; $p_\infty$is the far-field water partial pressure; p_i is the saturation vapour pressure above droplets in node i (corrected for the Kelvin effect); p_ice is the saturation vapour pressure above ice; T_∞ is the ambient gas temperature at locations far removed from the droplets; T_i^l and T_i^s are the surface temperatures of the water droplets and ice particles, respectively. It is assumed that $T_\infty=T_i^l=T_i^s$, because the gain or release of heat by particles during condensation/deposition or evaporation will not change the particle surface temperatures by more than 0.1 K (Chelf and Martin, 2001).

The dependence of the gas-phase diffusion coefficients, $D_v^*(r_i^l)$ and $D_v^*(r_i^s)$, on the radii of water and ice particles follows from the approach of Fuchs, which corrects for discontinuities in the vapour density above the particles when their radii approach the mean free path, λ, of vapour particles (Pruppacher and Klett, 1998):

$$D_v^*(r_i^{l/s})=\frac{D_v}{\left[\frac{r_i^{l/s}}{r_i^{l/s}+\Delta v}+\frac{D_v}{r_i^{l/s}\alpha_\mathrm{w/ice}}\left(\frac{2\pi M_\mathrm{w}}{RT_i^{l/s}}\right)^2\right]} \quad (8)$$

In the above expression, D_v is the vapour diffusivity of water in air, Δv is the distance of the vapour continuum above the particle surface (taken as 1.3 λ in the present study),

and α_w and α_{ice} are the mass accommodation coefficients for the evaporation of liquid droplets (evaporation coefficient) and vapour deposition on ice particles (deposition coefficient), respectively.

The values of α_w and α_{ice} required for computation of the corrected diffusion coefficients $D_v^*(r_i^l)$ and $D_v^*(r_i^s)$are not well known. Under temperature conditions characteristic of our freezing experiments, previously reported values of α_w vary from 0.04 to approximately 0.5 (Li et al., 2001; Shaw and Lamb, 1999), while those of α_{ice} span three orders of magnitude from approximately 0.001 to 0.6 (Choularton and Latham, 1977; Haynes et al., 1992; Magee et al., 2006; Pratte et al., 2006). Therefore, α_w and α_{ice} are treated as adjustable parameters in the model, and are iteratively varied during the minimization procedure (Sect. 3.2).

The far-field water partial pressure,p_∞, is calculated from the total concentration of gaseous water molecules (vapour), N_v, using the ideal gas law:

$$p_\infty = N_v\, kT_\infty \tag{9}$$

The value of N_v is determined by assuming that the concentration of gaseous water is in a steady-state with respect to condensation and evaporation to and from liquid droplets and deposition on ice particles, and is subject to losses to the ice-coated tube walls and fins.

$$\frac{dN_v}{dt} = -\sum_{i=1}^{96}\left(\frac{1}{v_w\rho_w}\frac{dm_i^l}{dt} + \frac{1}{v_{ice}\rho_{ice}}\frac{dm_i^s}{dt}\right) - k_{loss}\left(N_v - N_v^{ice}\right) \tag{10}$$

The two terms in the summation represent the contributions from the liquid droplets and ice particles, where m_i^l is the mass concentration of liquid droplets in node i, m_i^s is the mass concentration of ice particles in node i, and v_w and v_{ice} are the molecular volumes of liquid water and ice, respectively. The rates of change of mass concentration for liquid and ice particles in node i due to mass transfer are given by:

$$\frac{dm_i^l}{dt} = 4\pi r_i^{l^2}\rho_w N_i^l \frac{dr_i^l}{dt} \tag{11}$$

$$\frac{dm_i^s}{dt} = 4\pi r_i^{s^2}\rho_{ice} N_i^s \frac{dr_i^s}{dt} \tag{12}$$

The final term in Eq. (10) represents the loss of gaseous water to the ice-coated tube walls and fins, where N_v^{ice} is the concentration of vapour molecules given by the saturation vapour pressure of ice, and k_{loss} is the first-order rate constant for radial diffusion to the walls in a laminar flow (Houzelot and Villermaux, 1977; Villermaux, 1971):

$$k_{loss} = \frac{\mu D_v}{r_t^2} \tag{13}$$

In Eq. (13), μ=3.66 is the Sherwood number for a cylindrical pipe, and r_t is the tube radius. In the present study, k_{loss}=0.138 s^{-1} (Khalizov et al., 2006b).

From Eqs. (6) and (7), the changes in size of liquid water droplets and ice particles are determined by the difference between the far-field vapour pressure and the saturation vapour pressures of particles. The number of particles in a node may change due to size changes of particles resulting from condensation/deposition growth and evaporation. This exchange among nodes was implemented in the model using the approach of Prakash et al. (2003), in which the change in the number of liquid droplets in each node i is considered in terms of four vapour pressure scenarios:

$$\frac{dN_i^l}{dt} = \begin{cases} \frac{1}{(v_i - v_{i-1})\rho_w}\frac{dm_{i-1}^l}{dt} & \text{if } p_\infty > p_{i-1} \text{ (growth in bin } i-1) \\ -\frac{1}{(v_{i+1} - v_i)\rho_w}\frac{dm_{i+1}^l}{dt} & \text{if } p_\infty < p_{i+1} \text{ (evaporation in bin } i+1) \\ -\frac{1}{(v_{i+1} - v_i)\rho_w}\frac{dm_i^l}{dt} & \text{if } p_\infty > p_i \quad \text{(growth in bin } i) \\ \frac{1}{(v_i - v_{i-1})\rho_w}\frac{dm_i^l}{dt} & \text{if } p_\infty < p_i \quad \text{(evaporation in bin } i) \end{cases} \tag{14}$$

where v_i is the volume of a particle in node i, and v_{i-1} and v_{i+1} are the volumes of particles in adjacent size bins. The first two terms in Eq. (14) will increase the number density of particles in node i, while the last two terms will decrease the number density.

An equivalent set of equations is used to describe the change in the number of ice particles in each node i:

$$\frac{dN_i^s}{dt} = \begin{cases} \frac{1}{(v_i^s - v_{i-1}^s)\rho_{\text{ice}}} \frac{dm_{i-1}^s dt}{-} \frac{1}{(v_{i+1}^s - v_i^s)\rho_{\text{ice}}} \frac{dm_i^s}{dt} & \text{if } p_\infty > p_{\text{ice}} \text{ (growth)} \\ -\frac{1}{(v_{i+1}^s - v_i^s)\rho_{\text{ice}}} \frac{dm_{i+1}^s}{dt} + \frac{1}{(v_i^s - v_{i-1}^s)\rho_{\text{ice}}} \frac{dm_i^s}{dt} & \text{if } p_\infty < p_{\text{ice}} \text{ (evaporation)} \end{cases} \quad (15)$$

There are only two possibilities in this case, because p_{ice} is a function of temperature only, and does not vary for adjacent nodes.

The initial inputs for the microphysics component are the initial volume distribution of supercooled droplets, the time evolution of temperature (determined from the flow velocity and axial temperature profile, as described in Sect. 2.4), the first guesses of values of A_V and B_V for the calculation of the nucleation rate (Eq. 5), and the mass accommodation coefficients α_{w} and α_{ice} for the calculation of mass transfer by evaporation/growth. By performing the steps implied by Eqs. (2) to (15), the model calculates the time evolution of the far-field partial pressure, the number fraction of droplets frozen (ratio of number of droplets frozen to initial number of droplets), and thereby the evolution of the supercooled water and ice distributions.

3.2 Minimization component

The minimization procedure iteratively varies the values of A_V, B_V, α_{w} and α_{ice} to minimize the normalized sum of squares of differences, χ (Eq. 6 below), between the final volume distributions of supercooled water and ice aerosol particles measured in freezing experiments and those calculated by the model.

$$\chi = \frac{\sum_{i=1}^{96} \left(V_i^{l,\text{exp}} - V_i^{l,\text{calc}}\right)^2 + \sum_{i=1}^{96} \left(V_i^{s,\text{exp}} - V_i^{s,\text{calc}}\right)^2}{\left(\sum_{i=1}^{96} \left(V_i^{l,\text{exp}} + V_i^{s,\text{exp}}\right)\right)^2} \quad (16)$$

In the above equation, V_i^l and V_i^s are the volume densities of liquid droplets and ice particles, respectively, in node i. The additional superscripts indicate whether volume densities are from experimental (exp) or calculated (calc) distributions. The model can be run for a single freezing experiment at a given candidate freezing temperature, or for several freezing experiments, performed at different candidate freezing temperatures, simultaneously. In the latter case, χ is evaluated separately for each experiment using Eq. (16), and then averaged over all of the experiments. In either case, the model iteratively varies a single set of A_V, B_V, α_{w}, and α_{ice} values for all of the constituent experiments to minimize the final (averaged) value of χ.

The minimization component uses the *fminsearch* minimizer from the Matlab standard library, which finds a minimum for an unconstrained multivariable function using the simplex search method (Lagarias et al., 1998). The strong temperature dependence of homogeneous nucleation rates complicates the minimization, as A_V and B_V pairs producing reasonable values of J_V for a given temperature form a narrow strip on a plot of A_V versus B_V. Lines of constant J_V are given by $A_V = B_V T - C$, where C is a constant. If one changes A_V and B_V by moving along such a line, J_V does not change (for a given temperature), but its temperature dependence does. If, on the other hand, one moves perpendicular to such a line, J_V changes exponentially, while its temperature dependence changes little. This situation necessitates the use of extremely small steps in the minimization to maintain reasonable values of J_V, which slows down the calculation process dramatically.

To circumvent this issue, the parameters A_V and B_V were transformed to new parameters a_V and b_V, which allow the value of J_V and its temperature dependence to be changed independently, greatly enhancing the performance of the minimizer. The parameters a_V and b_V are the inclination and offset when J_V is approximated by a straight line on a $\log J_V$ versus T plot:

$$\log \frac{J_V}{J_0} = a_V (T - T_0) + b_V \quad (17)$$

where $J_0=1\,\mathrm{cm}^{-3}\,\mathrm{s}^{-1}$ provides the correct units. Changing a_V or b_V is equivalent to moving parallel or perpendicular, respectively, to the lines of constant J_V on the A_V versus B_V plot. The coordinate transformation is accomplished by developing $\log J_V(T)$ in a Taylor series expansion up to the first order, around a temperature T_0 within the freezing range typical for our freezing experiments:

$$a_V = \frac{1}{T_0 \ln 10}\left(1 + \frac{A_V}{kT_0}\right) \tag{18}$$

$$b_V = \frac{1}{\ln 10}\left(-\frac{A_V - B_V T_0}{kT_0} + \ln\frac{N_V kT_0}{hJ_0}\right) \tag{19}$$

For these experiments, a value of T_0=236.15 K was used. The new parameters a_V and b_V are used only in the minimization component of the model. In the microphysics component, a_V and b_V are transformed back to A_V and B_V, which are used to calculate J_V for each iteration.

4 Results and discussion

4.1 Changes in infrared spectra and aerosol size distributions upon cooling

Extinction spectra were recorded for pure water aerosol as a function of the candidate freezing temperature. The spectra obtained at 239.6, 236.3, 236.1, and 234.9 K are shown in Fig. 3 for the representative case of medium droplets produced by atomization. The freezing onset (homogeneous nucleation point) is indicated by distinct changes in the spectra between 236.3 and 236.1 K; specifically, broadening of the O-H vibrational stretching feature at $\sim$3000 cm^{-1} and the H-O-H bending feature at $\sim$1640 cm^{-1}. These changes become more pronounced when the temperature is reduced to 234.9 K and a larger number of droplets are frozen, with the O-H stretching

feature exhibiting a marked change in shape. In addition, the H-bonding (librational) feature at $\sim$700 cm^{-1} sharpens and shifts to higher wavenumbers.

The above changes in absorption features associated with freezing are all in accordance with previous reports (Cziczo and Abbatt, 1999; Clapp et al., 1995). Small variations in these spectral features at warmer temperatures are also evident from comparison of the spectra at 239.6 and 236.3 K. In fact, there is a general trend of spectra displaying more "ice-like" character as the temperature is decreased from near 273 K toward the nucleation point. A previous study in our laboratory (Zasetsky et al., 2004b) attributed these changes to the formation of low-density domains, consisting of ice-like clusters of water molecules, within the supercooled droplets.

The changes in extinction that occur above about 4000 cm^{-1}, where neither water nor ice absorb, are due to variations in scattering. After ice nucleation has occurred in a small fraction of supercooled droplets, the changes in slope in this region are due primarily to the growth of nascent ice particles by vapour diffusion from the remaining liquid droplets. The growth process can be characterised by retrieving temperature-dependent size distributions of supercooled water and/or ice aerosol particles from experimental spectra using the procedure outlined in Sect. 2.2.

Retrieved volume size distributions of hydrometeors are shown in Fig. 4 for the same set of freezing experiments using medium droplets. The spectra calculated from these retrieved size distributions are overlaid on the experimental spectra in Fig. 3. Figure 4 shows that the sample at 239.6 K was composed entirely of supercooled water, with the mode at a radius of $\sim$1.7 μm. The apparent contribution from small ice particles with radius approximately equal to that of the water droplets is believed to arise because the refractive indices, and therefore the spectra, of supercooled water and ice are very similar. Hence, experimental noise in the measured spectra and/or inaccuracies in the indices of refraction can introduce small uncertainties in the retrieved ice and water distributions (Zasetsky et al., 2004a). Similar small ice features are observed in the distributions at 236.1 K and 234.9 K, as well as at warmer temperatures (not shown). Since these features are not believed to represent ice, and comprise only a

small fraction of the total volume, they are removed from the distributions prior to their use in the microphysics model.

The secondary liquid water and ice features present at larger radii in Fig. 4 (e.g. the water peaks in the vicinity of 10 μm at 239.6 K and 236.1 K and the "tails" on the water and ice distributions at the largest radii) are also removed before model analysis. These features can potentially result from aerosol particles at large radii; however, the freezing of such large droplets would occur rapidly, and as such, is not pertinent to the present analysis, in which nucleation and mass transfer processes are considered over longer timescales (see Sect. 4.3). Large particle features in the distributions can also result from a baseline shift of the spectrometer (Zasetsky et al., 2004a). In either case, the features removed from the distributions make up less than 10% of the total volume.

The samples at 236.3 and 236.1 K in Fig. 4 were partially frozen, with maxima in the ice distributions at approximately 7.1 and 5.6 μm, respectively, while the sample at 234.9 K was completely frozen, with a maximum in the ice distribution at about 3.2 μm. The residual water apparent in the distributions at 234.9 K is attributed to the similarity of refractive indices for supercooled water and ice considered above, and is removed for subsequent analysis. The significant increases in the sizes of the ice particles relative to the initial supercooled water droplets are caused by deposition growth of the nucleated ice particles. The decrease in the size of the ice particles with reduction in temperature is a result of the temperature dependence of the growth process. Mass transfer is most significant near the nucleation point, where only a small fraction of the droplets have frozen and the saturation vapour pressure of water is high. As the temperature is reduced, the saturation vapour pressure of water decreases and a larger fraction of droplets freeze homogeneously, reducing the available liquid water for mass transfer and suppressing the growth of the ice particles.

It is important to emphasize that even for the completely frozen sample at 234.9 K, ice nucleated in only a small fraction of the droplets, and these then grew significantly by mass transfer. Further decreases in the candidate freezing temperature to 233.5 and 232.4 K led to the nucleation of a larger fraction of the droplets, which did not

grow as much as those at higher temperatures. The ice particle modes for these lower temperature cases (not shown) were at radii of 2.1 and 1.9 μm, respectively. At temperatures below 230 K, the size distribution of the ice particles corresponds approximately to that of the initial size distribution of supercooled water, indicating that homogeneous nucleation predominates and liquid-to-solid mass transfer growth is not significant. This is the expected consequence of the strong temperature dependences of both the nucleation rate and the mass transfer growth rate.

4.2 Nucleation temperature determination from retrievals

The volume size distributions of supercooled water and ice were used to calculate the volume fraction of ice – defined as the integrated volume concentration of ice particles divided by the sum of the integrated volume concentrations of ice and water particles – formed at each candidate freezing temperature. The resulting freezing curves for aerosol particles of each initial size are shown in Fig. 5. The curves for small and medium droplets overlap (dashed black line), and are shifted to slightly warmer temperatures than that for large droplets (solid grey line). We define the temperature at the mid-point of the curve, where the volume fraction of ice is 0.5, to be the homogeneous nucleation point. For each particle size, the nucleation temperature is approximately 236 K, in excellent agreement with values from previous work (Anderson et al., 1980; Cziczo and Abbatt, 1999; Demott and Rogers, 1990). Errors in the volume fraction frozen range from 2 to 3% in the plateau regions, where the samples are predominantly supercooled droplets or ice, to 10% near the nucleation point, where the phase composition is most sensitive to small fluctuations in temperature. Based on the latter, the upper limit for errors in the volume fraction of ice is illustrated by the error bar in Fig. 5.

The dependence of the volume fraction of ice on the candidate freezing temperature shows the evolution of the freezing process. However, the competition between homogeneous nucleation and mass transfer complicates the determination of the nucleation rate from these data, because the change in the volume of ice particles results from

both processes. To isolate the contribution of homogeneous nucleation from that of mass transfer growth so that the nucleation rate coefficients could be calculated, it was necessary to use a microphysical model (see Sect. 3) that contained both processes.

4.3 Nucleation rate determination from model simulations

Freezing experiments performed at different candidate freezing temperatures corresponded to different cross-sectional, mass-averaged temperature profiles obtained from a combination of direct measurements and high resolution CFD simulations (Sect. 2.4). Each experiment was interpreted in a separate model run. The input data for each run consisted of the measured initial and final supercooled water and/or ice aerosol particle distributions, the temperature profile, and the initial guesses for the parameters A_V, B_V, α_w and α_{ice}. An example of the evolution of the volume distributions of supercooled water and ice that the model obtains for a freezing experiment performed at a candidate freezing temperature of 235.7 K is shown in Fig. 6 for medium-sized droplets generated by atomization. The corresponding temperature profile and evolution of the far-field pressure (Eq. 9), the number fraction of droplets nucleated, and volume fraction of ice (determined from the distributions) are given in Fig. 7.

The initial volume distribution of supercooled water droplets in Fig. 6 (solid green curve) has a maximum at a radius of ~1.7 μm. As the aerosol travels to a region of lower temperature (Fig. 7), the volume density of water droplets decreases while that of ice particles increases. Figure 6 shows that the ice particles become larger due to mass transfer following freezing; the mode radii are 2.9 and 3.7 μm after residence times of 11.6 and 23.1 s, respectively. The final sample, calculated for a 34.7 s residence time, is composed almost entirely of ice particles (red dashed line; mode radius of 4.2 μm), with some residual water droplets.

The freezing experiment shown in Fig. 6 exemplifies a "partially frozen" case in which some liquid water droplets remain in the aerosol when it crosses the infrared detection beam. This corresponds to the vertical part of the freezing curve in Fig. 5, for which the volume fractions of ice are less than unity. Because water and ice are present

simultaneously, these partially frozen experiments are preferable to cases where all of the water droplets freeze before detection in the lowermost section of the flow tube. In the absence of liquid water droplets, the kinetic timescale over which nucleation occurred is uncertain, and the mass accommodation coefficients required for the correct description of diffusion-limited mass transfer cannot be properly constrained. Accordingly, subsets of experiments with partially frozen aerosols for each initial droplet size were selected for subsequent model analysis: three experiments for small droplets at different candidate freezing temperatures, five experiments for medium droplets, and three experiments for large droplets.

Because ice particle growth by mass transfer is significant for partially frozen samples, the model runs corresponding to these experiments should be sensitive to the values of the mass accommodation coefficients α_w and α_{ice}, which determine the magnitudes of the gas-phase diffusion coefficients $D_v^*(r_i^l)$ and $D_v^*(r_i^s)$, respectively (see Sect. 4.1). To demonstrate this sensitivity, a series of model runs were performed in which the values of α_w and α_{ice} were varied independently to find their influence on the value of χ. The results for the experiment with partially frozen, medium-sized droplets at 235.7 K are shown in Fig. 8. In this case, the best fit between the measured and calculated ice and water size distributions (minimum value of χ) was obtained with α_w=0.020 and α_{ice}=0.038. The trends displayed in Fig. 8 are representative of those observed for aerosols with smaller and larger droplet sizes. The steeper minimum in χ as a function of α_{ice} indicates that the results are more sensitive to changes in the accommodation coefficient on ice than to changes in α_w. The variations in Fig. 8 show that these experiments can be used to estimate the mass accommodation coefficients – at least under our experimental conditions.

Fits to experimental distributions calculated from model runs for supercooled droplets with a mode radius of 1.7 μm (medium-sized droplets) are shown in Fig. 9. The distributions producing the minimum value of χ are shown in each case. The associated values of J_V, calculated from the resulting values of A_V and B_V, are plotted in Fig. 10.

As seen in the lower panel of Fig. 7, the largest number of droplets nucleates in a narrow range of temperatures (~0.25 K) above the lowest temperature to which the particles are exposed in the AFT. This is due to the very strong temperature dependence of J_V, which changes by about two orders of magnitude per degree Kelvin (see Fig. 10). To obtain values of J_V over as wide a temperature range as possible, all five of the partially frozen experiments for medium droplets were fitted simultaneously, using a single set of minimization parameters. The result of this group fit is plotted as the solid curve in Fig. 10, showing the temperature dependence of the nucleation rate assuming that nucleation occurs within the droplet volume for samples in which most droplets have radii at or about 1.7 μm. Strictly speaking, this $J_V(T)$ curve applies only over the temperature range from 234.8 K to 236.2 K; that is, from the minimum temperature in the experiment performed at the lowest AFT wall temperature of 235.3 K to 0.25 K warmer than the minimum temperature in the experiment conducted at the highest wall temperature of 236.5 K (see Fig. 10). It should be noted that the minima in the temperature profiles are slightly lower than the set-point (average) wall temperatures because of the cooling configuration, which is responsible for the ±0.5 K axial gradient along tube sections.

Model fits to retrieved volume distributions from experiments with partially-frozen samples of small and large droplets, with mode radii of 1 and 2.9 μm, respectively, are shown in Fig. 11. The corresponding $J_V(T)$ curves obtained from group fits to experiments for each droplet size are plotted in Fig. 12. The valid temperature ranges for $J_V(T)$ are 235.0 to 235.8 K for small droplets and 234.8 to 235.8 K for large droplets. The $J_V(T)$ curve derived from the group fit to medium droplet experiments (Fig. 10) is plotted alongside those for small and large droplets in Fig. 12.

The values of χ, A_V, B_V, α_w and α_{ice} obtained from the group fits for each droplet size are given in Table 1. The values of A_V and B_V can be used in Eq. (5) to calculate values of $J_V(T)$, the temperature-dependent volume nucleation rate constant, over the temperature range of our experiments. Averaging the compiled values of mass accommodation coefficients, weighted by the number of freezing experiments used in each

group fit, results in α_w=0.054 and α_{ice}=0.031.

4.4 Comparison of nucleation rate coefficients

Values of $J_V(T)$ from previous studies of droplets created in an expansion chamber (Demott and Rogers, 1990) and levitated in a cooled electrodynamic balance (Duft and Leisner, 2004; Krämer et al., 1999; Stöckel et al., 2005) are plotted in Fig. 12 for comparison. The water droplets examined in these experiments ranged in size from about 5 to 50 μm. The values of $J_V(T)$ determined in the present study agree well with those of Stöckel et al. (2005) in terms of both temperature dependence and magnitude, essentially extending their values to lower temperatures. The temperature dependence of our results is similar to that obtained by Krämer et al. (1999) – which is supported by the results of Duft and Leisner (2004) – and to that of the curve of Pruppacher (1995), but the absolute values are somewhat lower. The Pruppacher recommendation is a fit to earlier experimental data, including those of DeMott and Rogers (1990), which agree with our values at low temperature, but have a different temperature dependence.

The droplet radii in each of the previous studies considered above are larger than the ~4 μm threshold for surface nucleation proposed by Duft and Leisner (2004). The droplet size distributions in the present study, however, all have mode radii below this threshold, allowing one to consider the applicability of classical nucleation theory for such droplets. In addition, all experiments in this study were performed in the same experimental apparatus under similar experimental conditions, allowing one to assess the size dependence of $J_V(T)$ with minimal contribution from systematic errors.

For a classical, volume-based freezing process, the nucleation rate depends on the droplet volume (function of r^3), and the rate coefficient $J_V(T)$ should be independent of droplet radius. This is not the case for the $J_V(T)$ curves for small, medium, and large droplets in the present study. It is evident from Fig. 12 that for these curves, the magnitude of $J_V(T)$ increases with decreasing droplet radius for a given temperature. This size dependence can potentially be attributed to the contribution of surface nucleation to the total nucleation rate, as considered in Eq. (1). As the droplet size decreases,

the surface-to-volume ratio increases, which could increase the contribution from J_S. These results suggest that classical nucleation theory cannot adequately describe the freezing of small, micrometre-sized supercooled water droplets, consistent with previous considerations of a droplet size threshold for surface nucleation (Duft and Leisner, 2004).

5 Conclusions

The freezing of micrometre-sized water aerosol droplets with mode radii of 1.0, 1.7, and 2.9 μm was studied as a function of temperature in a cryogenic AFT apparatus. Analysis of experimental extinction spectra using a previously-reported characterization procedure provided the size distributions and phase composition of the aerosol samples. The temperature dependence of the volume fraction of ice formed in the samples indicated a homogeneous nucleation point of approximately 236 K for each droplet size, in good agreement with previous literature reports.

An aerosol microphysics model was used to determine values of the temperature-dependent, volume-based homogeneous nucleation rate coefficient, $J_V(T)$, from experimental measurements. Mass accommodation coefficients for water molecules on liquid water, α_w, and ice, α_{ice}, were obtained from the model fits to experimental measurements. The fits were particularly sensitive to the value of α_{ice}, which is a key parameter in cloud models (e.g. Cotton et al., 2007; Jensen et al., 1998) because it influences the value of the vapour-phase diffusion coefficient, and thus the rate of ice particle growth via mass transfer. Mass accommodation coefficients from model fits to groups of experiments for each droplet size were averaged to obtain α_{w}=0.054 and α_{ice}=0.031.

The $J_V(T)$ curves determined for droplets with mode radii of 1.0, 1.7, and 2.9 μm show a distinct size dependence, with the magnitude of $J_V(T)$ increasing with decreasing droplet size. This indicates that the freezing of these droplets cannot be described solely using the classical, volume-based nucleation theory; rather, the contribution of

surface nucleation appears to increase with decreasing droplet size, reflecting higher surface-to-volume ratios. These results are consistent with the suggestion by Duft and Leisner (2004) that the surface nucleation rate could become comparable to the volume rate at radii below approximately 4 μm.

Surface nucleation of small droplets will modulate the formation of cirrus clouds, altering the concentrations and sizes of ice crystals that would be produced as compared to volume-only nucleation scenarios. This has potentially important ramifications for bulk parameterizations in numerical models, which typically employ temperature- and composition-dependent formulations for the homogeneous nucleation rate coefficient based solely on the classical, volume-based approach (Kärcher and Lohmann, 2002; Liu and Penner, 2005). Any contribution from a surface-based process will alter the predicted characteristics of ice formation and growth, and in turn, the predicted cloud microphysical and radiative properties. Further work is required to develop a size-dependent parameterization for homogeneous nucleation that accounts for both volume- and surface-based processes, as considered in a related manuscript (Kuhn et al., 2009).

Acknowledgements. This research was supported by the Natural Sciences and Engineering Research Council of Canada, the Canadian Foundation for Climate and Atmospheric Science, and the Ontario Research and Development Challenge Fund. The authors would also like to thank Alex Zasetsky for invaluable input throughout this project, Brendan Pinto and Monica Harvey for assistance with the experimental measurements and microphysics model, and Wayde Johnson for conducting the CFD analysis of our AFT.

References

Anderson, R. J., Miller, R. C., Kassner, J. L., and Hagen, D. E.: A study of homogeneous condensation-freezing nucleation of small water droplets in an expansion cloud chamber, J. Atmos. Sci., 37, 2508–2520, 1980.

Bohren, C. F. and Huffman, D. R.: Absorption and Scattering of Light by Small Particles, John Wiley and Sons, Inc., New York, 530p., 1983.

Butorin, G. T. and Skripov, V. P.: Crystallization in supercooled water, Kristallografiya, 17, 379–384, 1972.
Chelf, J. H. and Martin, S. T.: Homogeneous ice nucleation in aqueous ammonium sulfate aerosol particles, J. Geophys. Res., 106, 1215–1226, 2001.
Choularton, T. W. and Latham, J.: Measurements of deposition coefficient for ice, and its application to cirrus seeding, Q. J. Roy. Meteorol. Soc., 103, 307–318, 1977.
Clapp, M. L., Miller, R. E., and Worsnop, D. R.: Frequency-dependent optical-constants of water ice obtained directly from aerosol extinction spectra, J. Phys. Chem., 99, 6317–6326, 1995.
Cotton, R. J., Benz, S., Field, P. R., Móhler, O., and Schnaiter, M.: Technical Note: A numerical test-bed for detailed ice nucleation studies in the AIDA cloud simulation chamber, Atmos. Chem. Phys., 7, 243–256, 2007, http://www.atmos-chem-phys.net/7/243/2007/.
Cziczo, D. J. and Abbatt, J. P. D.: Deliquescence, efflorescence, and supercooling of ammonium sulfate aerosols at low temperature: implications for cirrus cloud formation and aerosol phase in the atmosphere, J. Geophys. Res., 104, 13781–13790, 1999.
Demott, P. J. and Rogers, D. C.: Freezing nucleation rates of dilute-solution droplets measured between −30-degrees-C and −40-degrees-C in laboratory simulations of natural clouds, J. Atmos. Sci., 47, 1056–1064, 1990.
Djikaev, Y. S., Tabazadeh, A., Hamill, P., and Reiss, H.: Thermodynamic conditions for the surface-stimulated crystallization of atmospheric droplets, J. Phys. Chem. A, 106, 10247–10253, 2002.
Duft, D. and Leisner, T.: Laboratory evidence for volume-dominated nucleation of ice in supercooled water microdroplets, Atmos. Chem. Phys., 4, 1997–2000, 2004, http://www.atmos-chem-phys.net/4/1997/2004/.
Glickman, T.: Glossary of meteorology, American Meteorological Society, Boston, 855p., 2000.
Haynes, D. R., Tro, N. J., and George, S. M.: Condensation and evaporation of H_2O on ice surfaces, J. Phys. Chem., 96, 8502–8509, 1992.
Heymsfield, A. J., Miloshevich, L. M., Schmitt, C., Bansemer, A., Twohy, C., Poellot, M. R., Fridlind, A., and Gerber, H.: Homogeneous ice nucleation in subtropical and tropical convection and its influence on cirrus anvil microphysics, J. Atmos. Sci., 62, 41–64, 2005.
Hinds, W. C.: Aerosol technology: properties, behavior, and measurement of airborne Particles, Wiley-Interscience, Toronto, 483p., 1999.
Houzelot, J. L. and Villermaux, J.: Mass-transfer in annular cylindrical reactors in laminar-flow,

Chem. Eng. Sci., 32, 1465–1470, 1977.
Hung, H. M., Malinowski, A., and Martin, S. T.: Ice nucleation kinetics of aerosols containing aqueous and solid ammonium sulfate particles, J. Phys. Chem. A, 106, 293–306, 2002.
Hung, H. M. and Martin, S. T.: Apparent freezing temperatures modeled for several experimental apparatus, J. Geophys. Res.-Atmos., 106, 20379–20394, 2001.
Jensen, E. J., Toon, O. B., Tabazadeh, A., Sachse, G. W., Anderson, B. E., Chan, K. R., Twohy, C. W., Gandrud, B., Aulenbach, S. M., Heymsfield, A., Hallett, J., and Gary, B.: Ice nucleation processes in upper tropospheric wave-clouds observed during SUCCESS, Geophys. Res. Lett., 25, 1363-1366, 1998.
Kärcher, B. and Lohmann, U.: A parameterization of cirrus cloud formation: homogeneous freezing of supercooled aerosols, J. Geophys. Res.-Atmos., 107, AAC 4-1–AAC 4-10, 2002.
Khalizov, A., Earle, M. E., Johnson, W. J. W., Stubley, G. D., and Sloan, J. J.: Development and characterization of a laminar aerosol flow tube, Rev. Sci. Instrum., 77, 033102, doi:10.1063/1.2175958, 2006a.
Khalizov, A. F., Earle, M. E., Johnson, W. J. W., Stubley, G. D., and Sloan, J. J.: Modeling of flow dynamics in laminar aerosol flow tubes, J. Aerosol Sci., 37, 1174–1187, 2006b.
Krämer, B., Hubner, O., Vortisch, H., Woste, L., Leisner, T., Schwell, M., Ruhl, E., and Baumgartel, H.: Homogeneous nucleation rates of supercooled water measured in single levitated microdroplets, J. Chem. Phys., 111, 6521–6527, 1999.
Kuhn, T., Earle, M. E., Khalizov, A. F., and Sloan, J. J.: Size dependence of volume and surface nucleation rates for homogeneous freezing of supercooled water droplets, Atmos. Chem. Phys. Discuss., 9, 22929–22953, 2009, http://www.atmos-chem-phys-discuss.net/9/22929/2009/.
Lagarias, J. C., Reeds, J. A., Wright, M. H., and Wright, P. E.: Convergence properties of the Nelder-Mead simplex method in low dimensions, Siam J. Optimiz., 9, 112–147, 1998.
Lawson, R. P., Baker, B. A., Pilson, B., and Mo, Q.: In situ observations of the microphysical properties of wave, cirrus, and anvil clouds, Part II: cirrus clouds, J. Atmos. Sci., 63, 3186–3203, 2006.
Li, Y. Q., Davidovits, P., Shi, Q., Jayne, J. T., Kolb, C. E., and Worsnop, D. R.: Mass and thermal accommodation coefficients of H_2O(g) on liquid water as a function of temperature, J. Phys. Chem. A, 105, 10627–10634, 2001.
Liou, K. N.: Influence of cirrus clouds on weather and climate processes: a global perspective, Mon. Weather Rev., 114, 1167–1199, 1986.

Liu, X. and Penner, J. E.: Ice nucleation parameterization for global models, Meteorol. Z., 14, 499–514, 2005.

Magee, N., Moyle, A. M., and Lamb, D.: Experimental determination of the deposition coefficient of small cirrus-like ice crystals near-50 degrees C, Geophys. Res. Lett., 33, L17813, doi:10.1029/2006GL026665, 2006.

Prakash, A., Bapat, A. P., and Zachariah, M. R.: A simple numerical algorithm and software for solution of nucleation, surface growth, and coagulation problems, Aerosol Sci. Tech., 37, 892–898, 2003.

Pratte, P., Van Den Bergh, H., and Rossi, M. J.: The kinetics of H2O vapor condensation and evaporation on different types of ice in the range 130–210 K, J. Phys. Chem. A, 110, 3042–3058, 2006.

Pruppacher, H. R.: A new look at homogeneous ice nucleation in supercooled water drops, J. Atmos. Sci., 52, 1924–1933, 1995.

Pruppacher, H. R. and Klett, J. D.: Microphysics of Clouds and Precipitation, Kluwer Academic Publishers, Boston, 954p., 1998.

Shaw, R. A. and Lamb, D.: Experimental determination of the thermal accommodation and condensation coefficients of water, J. Chem. Phys., 111, 10659–10663, 1999.

Stöckel, P., Weidinger, I. M., Baumgartel, H., and Leisner, T.: Rates of homogeneous ice nucleation in levitated H_2O and D_2O droplets, J. Phys. Chem. A, 109, 2540–2546, 2005.

Tabazadeh, A., Djikaev, Y. S., Hamill, P., and Reiss, H.: Laboratory evidence for surface nucleation of solid polar stratospheric cloud particles, J. Phys. Chem. A, 106, 10238–10246, 2002a.

Tabazadeh, A., Djikaev, Y. S., and Reiss, H.: Surface crystallization of supercooled water in clouds, P. Natl. Acad. Sci. USA., 99, 15873–15878, 2002b.

Taborek, P.: Nucleation in emulsified supercooled water, Phys. Rev. B, 32, 5902–5906, 1985.

Turnbull, J. and Fisher, J. C.: Rate of nucleation in condensed systems, J. Chem. Phys., 17, 71–73, 1949.

Villermaux, J.: Diffusion in a cylindrical reactor, Int. J. Heat Mass Transfer, 14, 1963–1981, 1971.

Zasetsky, A. Y., Earle, M. E., Cosic, B., Schiwon, R., Grishin, I. A., McPhail, R., Pancescu, R. G., Najera, J., Khalizov, A. F., Cook, K. B., and Sloan, J. J.: Retrieval of aerosol physical and chemical properties from mid-infrared extinction spectra, J. Quant. Spectrosc. Ra., 107, 294–305, 2007.

Zasetsky, A. Y., Khalizov, A. F., Earle, M. E., and Sloan, J. J.: Frequency dependent complex refractive indices of supercooled liquid water and ice determined from aerosol extinction spectra, J. Phys. Chem. A, 109, 2760–2764, 2005.

Zasetsky, A. Y., Khalizov, A. F., and Sloan, J. J.: Characterization of atmospheric aerosols from infrared measurements: simulations, testing, and applications, Appl. Optics, 43, 5503–5511, 2004a.

Zasetsky, A. Y., Khalizov, A. F., and Sloan, J. J.: Local order and dynamics in supercooled water: a study by IR spectroscopy and molecular dynamic simulations, J. Chem. Phys., 121, 6941–6947, 2004b.

Table 1. Minimization parameters from group fits for each droplet size.

Radius (μm)	χ	A_V (J)	B_V (J/K)	α_w	α_{ice}
1.0	$3.68{\cdot}10^{-3}$	$-2.592393{\cdot}10^{-18}$	$-1.186721{\cdot}10^{-20}$	0.054	0.030
1.7	$3.50{\cdot}10^{-3}$	$-2.527704{\cdot}10^{-18}$	$-1.159562{\cdot}10^{-20}$	0.063	0.030
2.9	$2.14{\cdot}10^{-3}$	$-2.386266{\cdot}10^{-18}$	$-1.100254{\cdot}10^{-20}$	0.039	0.032

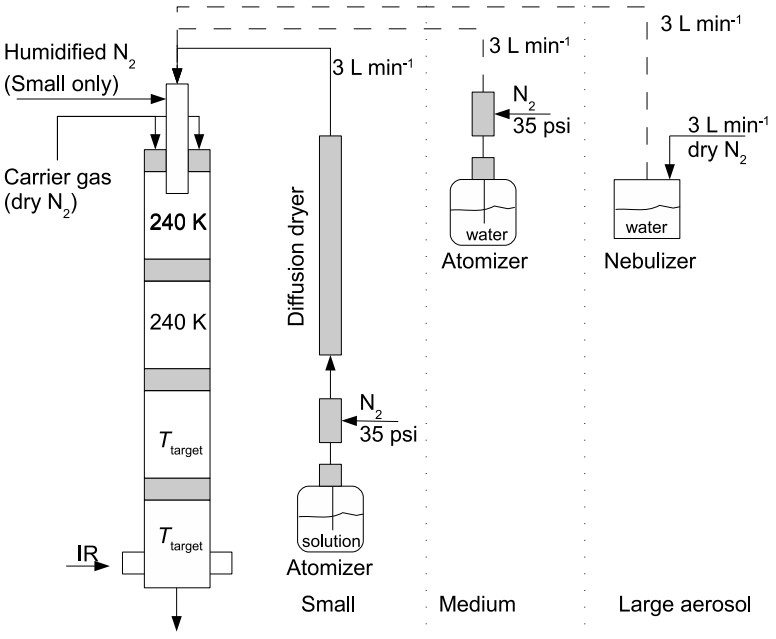

Fig. 1. Setup of cryogenic aerosol flow tube apparatus showing the three alternative configurations for aerosol generation.

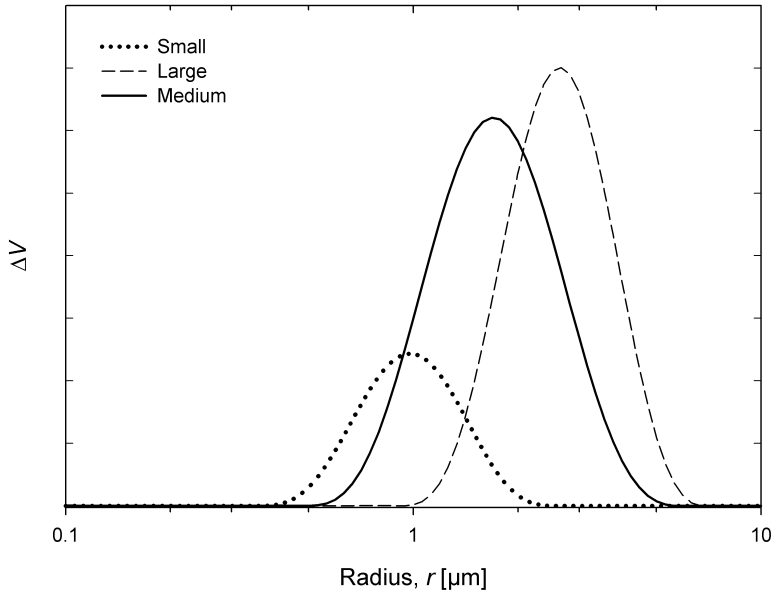

Fig. 2. Volume size distributions of supercooled water droplets after conditioning at 240 K. The droplets have mode radii of 1.0 μm (small), 1.7 μm (medium), and 2.9 μm (large), corresponding to the generation methods of heterogeneous condensation, atomization, and nebulization, respectively (Fig. 1).

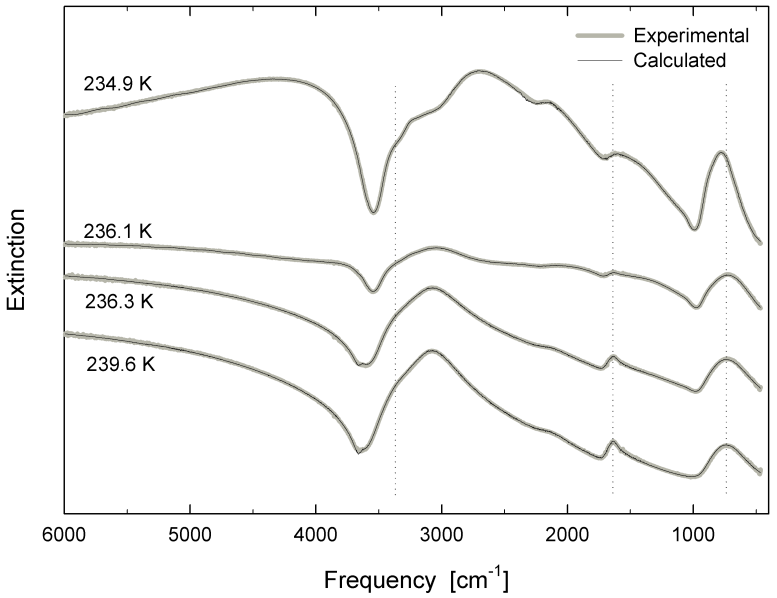

Fig. 3. Experimental extinction spectra obtained from freezing experiments using medium droplets generated by atomization at different candidate freezing temperatures. The spectra calculated from the retrieved size distributions are overlaid in black.

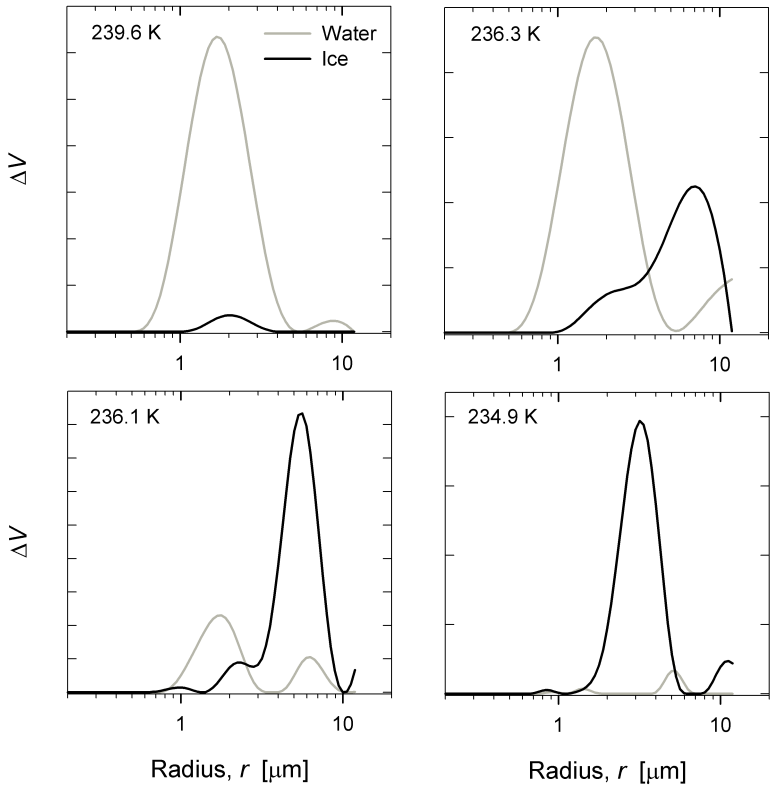

Fig. 4. Volume size distributions obtained using the aerosol retrieval procedure with the experimental spectra from freezing experiments using medium droplets in Fig. 3. The corresponding candidate freezing temperatures are indicated for the individual experiments.

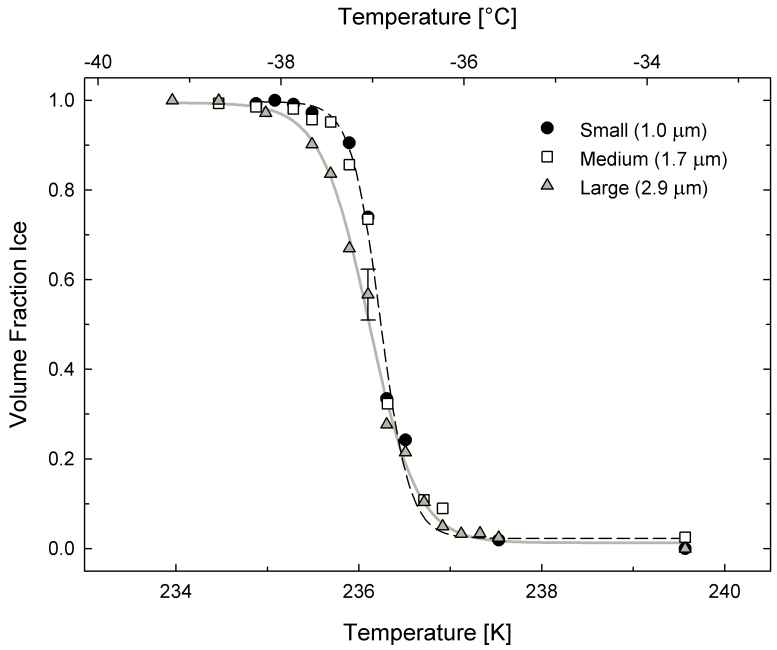

Fig. 5. Freezing curves determined from volume size distributions for experiments using each initial droplet size.

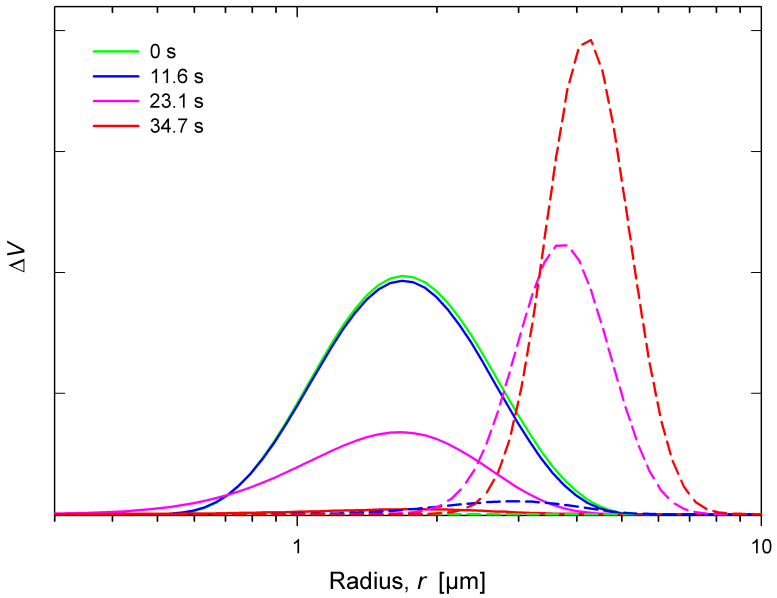

Fig. 6. Time evolution of volume distributions of supercooled water (solid lines) and ice (dashed lines) at 0, 11.6, 23.1, and 34.7 s for a sample model run for medium droplets at 235.7 K.

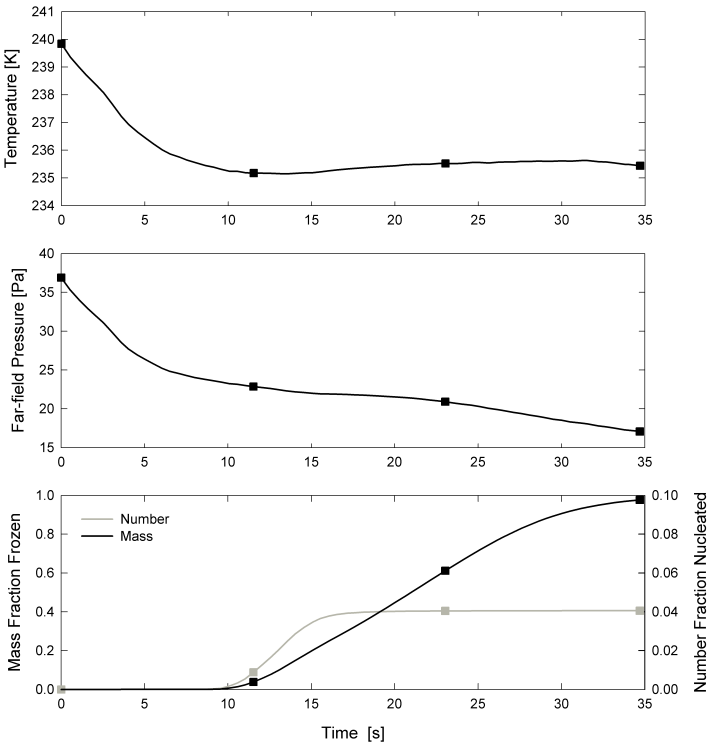

Fig. 7. Axial temperature profile and time evolution of far-field water vapour pressure, number fraction of droplets nucleated, and volume fraction of ice calculated by the model for the run at 235.7 K (medium droplets). The solid squares indicate the times for which the volume distributions of supercooled water and ice are shown in Fig. 6.

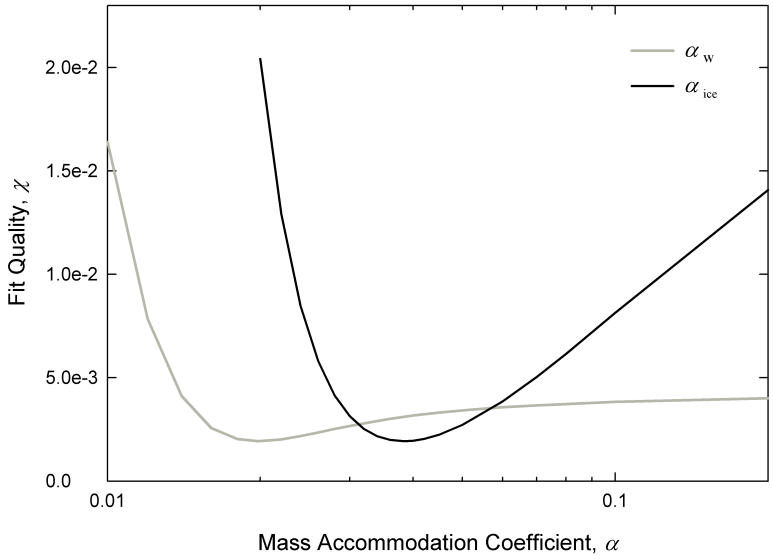

Fig. 8. Variation of χ with changes in mass accommodation coefficients α_w and α_{ice} for the representative case of a partially frozen experiment for medium droplets at 235.7 K.

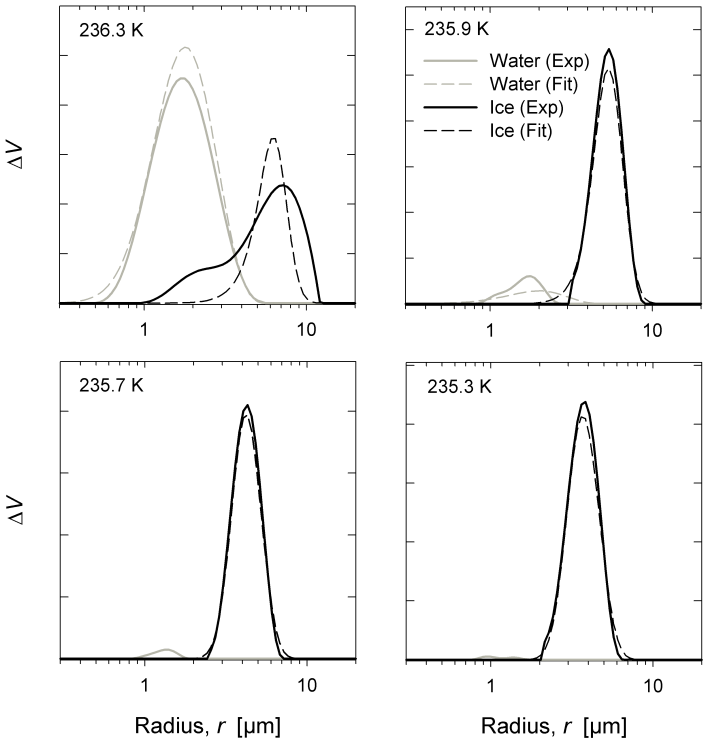

Fig. 9. Model fits to experimentally-measured distributions from partially frozen samples (medium droplets). The corresponding candidate freezing temperatures are indicated for the individual experiments.

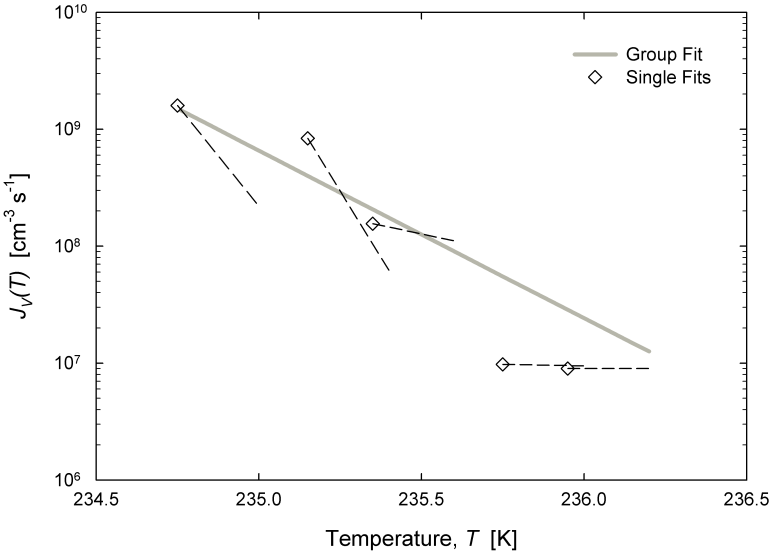

Fig. 10. Volume-based nucleation rate coefficients, J_V, determined from single and group fits to partially frozen experiments for medium droplets. The open diamonds indicate the lowest temperature reached in each freezing experiment, and the dashed lines show the temperature dependence of J_V to 0.25 K above the minimum temperature.

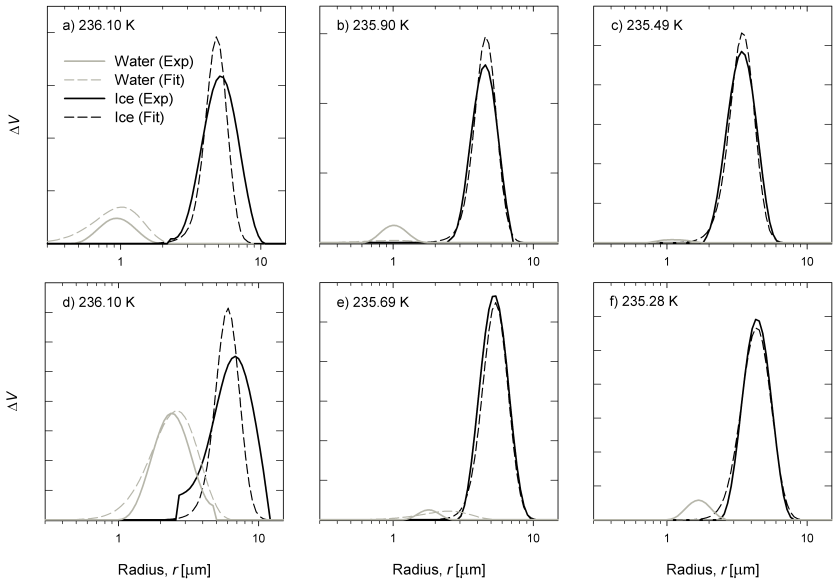

Fig. 11. Model results and comparison with experimentally measured size distributions for small and large droplets. The upper three panels **(a)** to **(c)** show results for the three experiments used in the small droplet group; the lower panels **(d)** to **(f)** the results of the large droplet group. The corresponding candidate freezing temperatures are indicated in the figure for the individual experiments.

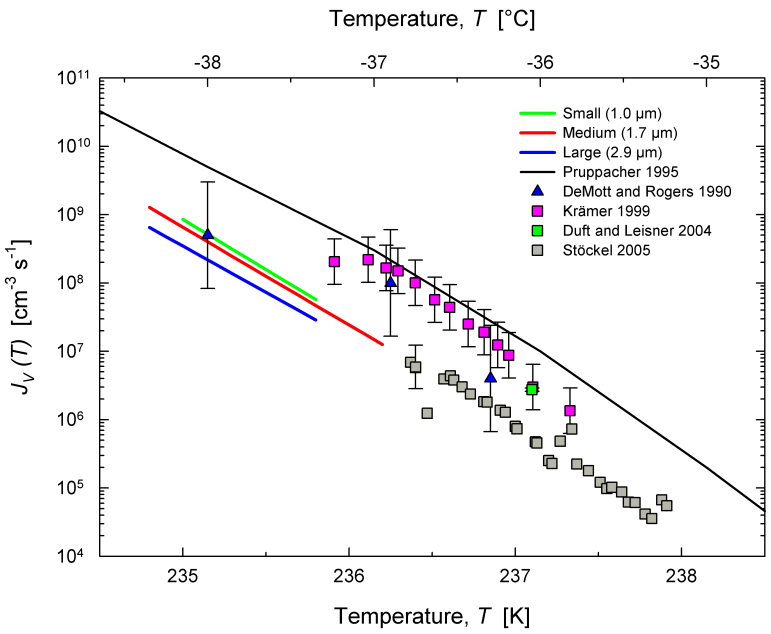

Fig. 12. Volume-based homogeneous nucleation rate coefficients, $J_V(T)$, determined from model fits to groups of experiments for small, medium, and large droplets. Literature values of $J_V(T)$ determined using levitated droplets in electrodynamic balances (squares) and expansion cloud chambers (triangles) are shown for comparison.